Original Research

In Vivo R1-Enhancement Mapping of Canine Myocardium Using CeMRI With Gd(ABE-DTTA) in an Acute Ischemia-Reperfusion Model

P. Kiss, MD,[1] P. Suranyi, MD,[1,3] T. Simor, MD, PhD,[1,3] N.H. Saab-Ismail, PhD,[1,3] A. Elgavish, PhD,[2,3*] L. Hejjel, MD,[1,3] and G.A. Elgavish, PhD[1,3*]

Purpose: To demonstrate the usefulness of normalized $\Delta R1$ ($\Delta R1_n$) mapping in myocardial tissue following the administration of the contrast agent (CA) Gd(ABE-DTTA).

Materials and Methods: Ischemia-reperfusion experiments were carried out in 11 dogs. The method exploited the relatively long tissue lifetime of Gd(ABE-DTTA), and thus no fast R1 measurement technique was needed. Myocardial perfusion was determined with colored microspheres (MP).

Results: With varying extent of ischemia, impaired wall motion (WM) and lower $\Delta R1_n$ values were detected in the ischemic sectors, as opposed to the nonischemic sectors where normal WM and higher $\Delta R1_n$ were observed. Based on the $\Delta R1_n$, data from the myocardial perfusion assay and the $\Delta R1_n$ maps were compared in the ischemic sectors. A correlation analysis of these two parameters demonstrated a significant correlation ($R = 0.694$, $P < 0.005$), validating the $\Delta R1_n$-mapping method for the quantitation of ischemia. Similarly, pairwise correlations were found for the MP, $\Delta R1_n$, and wall thickening (WT) values in the same areas. Based on the correlation between $\Delta R1_n$ and MP, $\Delta R1_n$ maps calculated with a pixel-by-pixel resolution can be converted to similarly high-resolution myocardial perfusion maps.

Conclusion: These results suggest that the extent of the severity of ischemia can be quantitatively represented by $\Delta R1_n$ maps obtained in the presence of our CA.

Key Words: myocardial ischemia; contrast agent; myocardial perfusion; MRI; RI mapping
J. Magn. Reson. Imaging 2006;24:571–579.

ISCHEMIC HEART DISEASE remains the leading cause of death in western societies (1). A noninvasive imaging method to visualize acute myocardial ischemia is highly desirable (2–4). The techniques currently used, such as contrast-enhanced (CE) cardiac ultrasound, technetium-99m-tetrafosmin single-photon emission computed tomographic (SPECT) imaging, and thallium-201 myocardial tomography, are not optimal for accurate localization or, more importantly, quantitative determination of myocardial underperfusion (5). Presently, coronary angiography provides the most accurate information for the differential diagnosis of acute myocardial ischemia. This method, however, carries significant risks and cannot be repeated as often as MRI (6,7). ceMRI can visualize myocardial ischemia with less risk (8,9); however, current cardiac ceMRI techniques could be improved regarding of spatial resolution and coverage. In this work we present results obtained by R1 mapping, which in conjunction with a contrast agent (CA) with a long lifetime in tissue, Gd(ABE-DTTA), provides quantitative pixel-by-pixel information on myocardial underperfusion.

In the differential diagnosis of acute myocardial ischemia, cardiac MRI has played an increasingly important role in visualizing perfusion abnormalities. With the use of blood oxygen level-dependent (BOLD) MRI, myocardial ischemia can be detected without using CAs (10). However, to precisely delineate the ischemic area in the myocardium, the use of MRI CAs is required (11–13). Based on differences in the distribution of a CA between healthy and ischemic regions, ceMRI should be able to detect and accurately assess myocardial underperfusion.

McNamara et al (14) used Gd-DTPA to detect myocardial ischemia in a canine heart model. Since then Gd-DTPA has remained the most frequently used MRI CA for detecting acute myocardial ischemia in clinical practice (15), although some investigators have used other agents in their experimental and human studies (16–21).

MRI CAs display wash-in and wash-out kinetics that reflect myocardial perfusion (MP) abnormalities (22). The application of a first-pass technique to detect myocardial ischemia in a rat heart model was reported by

[1]Department of Biochemistry and Molecular Genetics, University of Alabama at Birmingham, Birmingham, Alabama, USA.
[2]Department of Genetics, University of Alabama at Birmingham, Birmingham, Alabama, USA.
[3]Elgavish Paramagnetics Inc., Birmingham, Alabama, USA.
Contract grant sponsor: National Institutes of Health (NIH); Contract grant numbers: R44 HL58285; RO1 HL63340.
*Address reprint requests to: G.A.E., Department of Biochemistry and Molecular Genetics, University of Alabama at Birmingham, MCLM556, 1918 University Blvd., Birmingham, AL 35294-0005.
E-mail:gabi@uab.edu
Received September 15, 2005; Accepted May 5, 2006.
DOI 10.1002/jmri.20661
Published online 4 August 2006 in Wiley InterScience (www.interscience.wiley.com).

Atkinson et al (23). The same authors also visualized myocardial ischemia in patients with coronary disease by first-pass kinetics using Gd-DTPA (24). To date, this is the best MRI technique for detecting myocardial perfusion (24). However, first-pass techniques are not optimal in terms of spatial resolution and coverage due to short duration of contrast.

Signal intensity enhancement (SIE) is dependent on CA concentration in the myocardial volume element represented by the corresponding image area, but not in a linear fashion. SIE is not an intrinsic parameter; rather, it depends on the pulse sequence and acquisition parameters used. The intrinsic physical parameter that is enhanced in linear proportion with CA concentration is the paramagnetic relaxation rate enhancement, $\Delta R1$, which is the difference between the inverse T1 in the presence vs. the absence of CA. Using $\Delta R1$ to determine regional CA concentration liberates this determination from dependence on extraneous experimental factors (field inhomogeneities, preparation pulse errors, saturation, coil effect, etc.). The $\Delta R1$ obtained from a region of interest (ROI) that represents a given myocardial volume element actually represents the CA concentration averaged over that volume element. Thus, a $\Delta R1$ map of the heart in ceMRI is a faithful representation of CA distribution with a spatial resolution down to the voxel-by-voxel level.

To benefit most from ceMRI, several techniques were developed to investigate myocardial perfusion defects (25) and pathologies in brain (26) including first-pass perfusion imaging (24). However, the accuracy of perfusion detection with this method is limited because it utilizes MRI SIs. Since the SI of a given pixel in an MR image may be distorted by the factors detailed above, an SI-based image of the myocardium following CA administration may provide inaccurate quantitative information about the location and severity of myocardial underperfusion. Thus an R1-map-based approach would be preferable. Unfortunately, however, with the MRI instruments presently used in the clinic, the acquisition of images using inversion recovery (IR) for a typical R1 map currently requires 15 minutes of scanning time per tomographic slice. Thus, the myocardial lifetime of the CAs presently used in the clinic is too short to obtain an R1 map of the left ventricle (LV) with IR. To solve this problem we developed an agent that remains in tissue long enough to allow the generation of a R1 map.

We successfully applied this tissue-persistent myocardial CA, Gd(BME-DTTA), to a ferret myocardial ischemia model (27). Because of its relatively long lifetime in the myocardium, the contrast between the ischemic and nonischemic regions remained significant during the entire 30-minute ischemic period. Our current, related agent, Gd(ABE-DTTA) (28), retains the MRI qualities of Gd(BME-DTTA) but it is preferable over the latter because of improved water solubility. We used it successfully in previous studies to detect myocardial underperfusion (29,30). Its relatively long lifetime in the myocardium allows its use for R1 mapping of the entire LV.

MATERIALS AND METHODS

Canine Preparation

Eleven male mongrel dogs weighing 17–19 kg were used in our study. AcqKnowledge v3.7.2 software running on a Toshiba notebook PC connected to an MP100A (Biopac Systems Inc., CA, USA) was used to record ECG and pressure. Anesthesia was started with an initial I.V. bolus of sodium pentobarbital (25 mg/kg). The dogs were intubated and mechanically ventilated. Body temperature was maintained. An I.V. line was inserted to administer infusion and pentobarbital. Both femoral arteries were cannulated to obtain arterial blood samples during microsphere (Mø) injections and to monitor blood pressure. Blood pressure and ECG were continuously recorded. A left-side thoracotomy was performed. A 1-cm-long section of the left anterior descending coronary artery (LAD) was isolated from its bed. A silk tie was placed around the LAD to allow occlusion to create ischemia. The aperture of the thoracotomy was closed to restore roughly a normal anatomical situation. To ascertain whether the size of the ischemic region was large enough, a 20-second zero-flow ischemia test was performed, monitored by ECG.

Experimental Protocol

Control short-axis MR images were acquired, Mø of the first color were injected, and a blood sample was taken. Subsequently, zero-flow ischemia was created by pulling the ligature tight, and the CA was injected. At that time, Mø of the second color were injected and a blood sample was taken. Cine and IR MR images were collected starting at the 10th minute of the 30-minute ischemic period. At the end of the 30-minute period of ischemia, the LAD ligature was removed to allow 40 minutes of reperfusion. Mø of the third color were injected in the sixth minute of the reperfusion period, and a blood sample and MR images were taken. At the end of the reperfusion period the animals were euthanized. In Fig. 1 the timeline of our experimental protocol is illustrated.

Analysis of Myocardial Perfusion

The dogs hearts were excised, washed, and bread-sliced according to the anatomical orientation of the short-axis MR images (see below). Each slice was cut into eight or 16 pieces (depending on the mass of the actual slice) of approximately 1 g each. Each tissue sample was placed individually in a test tube that contained 1M KOH for digestion at 60°C for 12 hours. The blood samples were digested by 2M KOH. Further processing of tissue and blood samples was carried out as described by Simor et al (27) to calculate myocardial perfusion as determined by colored Mø.

CA

Agent Preparation

Gd(ABE-DTTA) (Fig. 2) was synthesized, and the samples were prepared as described by Saab at al (28). Each injectable sample of Gd(ABE-DTTA) was prepared by mixing solutions of Gd(ABE-DTTA) and Ca(ABE-DTTA)

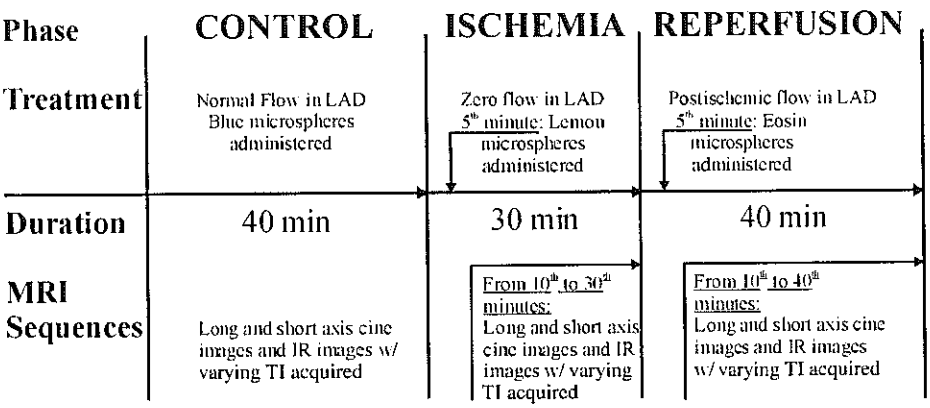

Figure 1. Timeline of the experimental protocol.

in a 10:3 ratio. For quality control, the relaxivity of each such sample was measured, and a relaxivity of 20 $sec^{-1} \cdot mM^{-1}$ (pH 6.4; 20°C, 8.5T) was routinely obtained.

Determination of Relaxivity

A determination of relaxivity was carried out for each injectable sample of CA to maintain quality control. The IR method was used to measure T1. A 180° preparation pulse was followed by a variable delay. The magnetization was then sampled by a second pulse, and the resulting free induction decay (FID) signal was acquired. The magnetization M_τ for any interpulse delay time τ is given by the equation:

$$M_\tau = M_{eq}(1 - A^{-R1\cdot\tau}) \quad (1)$$

where M_{eq} and R1 are the magnetization at equilibrium and the relaxation rate (R1 = 1/T1), respectively, and A is a constant that depends on the quality of the 180° pulse and the extent of signal saturation. Under ideal conditions, A = 2.0. For a series of delay times τ, FID intensities, or signal intensities when Fourier transformation is done, are generated and the data are fit to a curve described by Eq. [1]. A three-parameter, no-constraint fit is carried out and the R1 is obtained from the best fit. These measurements were carried out on an Avance (360 MHz, 8.5T) Bruker NMR spectrometer. For each sample, R1 is calculated from three consecutive measurements.

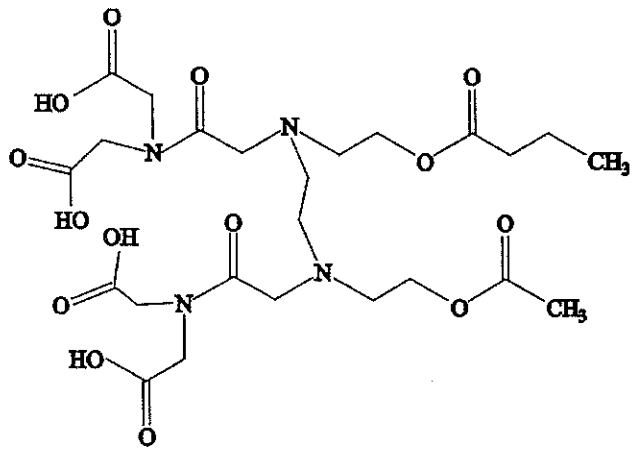

(ABE-DTTA)

Figure 2. Ligand of the CA, Gd(ABE-DTTA).

MRI

Slice Orientations

A seven-slice short-axis image grid was positioned on the end-diastolic image of a four-chamber, long-axis, steady-state-free-precession (SSFP) movie. The seven short-axis tomographic slices were positioned starting from the level of the aortic valve. A slice thickness of 10 mm was chosen so that the seven slices would cover the entire LV from apex to base. The duration of the 30-minute ischemia was insufficient to cover the entire LV. Thus, based on the anatomic position of the ligature of LAD, only one of these seven slices was chosen to determine R1. Cine MRI, however, was acquired covering the entire LV.

Normalized ΔR1 Mapping

An IR prepared segmented fast gradient-echo sequence was used on a 1.5 Tesla GE Signa Horizon CV instrument to determine R1. R1 values were obtained using the IR method employing eight different TI values. Short-axis IR images were obtained with the following parameters: 260-mm FOV, 256 × 256 image matrix, 25° readout flip angle, and 3.32-msec echo time (TE). TR was determined by the actual heart rate (TR = 3 cardiac cycles). The acquisition of all TIs was timed to the end-diastolic phase of the cardiac cycle.

The R1 values for each ROI were calculated by curve-fitting from the TI-dependent SIs using (31):

$$SI = SI_0(1 - A\cdot e^{-TI\cdot R1} + e^{-TR\cdot R1}) \quad (2)$$

Where SI stands for the observed signal intensity, SI_0 is the signal intensity at equilibrium, TI is the inversion time, and A is a parameter ($A \leq 2$) obtained by the curve-fitting procedure. The rightmost exponential term corrects for signal saturation (31).

Two alternative postacquisition calculations with two different spatial resolutions were carried out: 1) R1 values were calculated for each myocardial sector serving as ROI according to the physical sectors in which myocardial perfusion was determined using MPs, and 2) R1 values were calculated with a voxel-by-voxel resolution (each voxel as an ROI) exploiting the maximum spatial resolution potential provided by the equipment and the imaging pulse sequence.

Myocardial Function

To determine myocardial function, cine MR images were acquired using an SSFP sequence. The applied parameters were as follows: 260-mm FOV, 128 × 128 image matrix, and 45° flip angle.

Image Analysis

MR Analytical Software System (MASS) version 5.0 (Medis, Leiden, The Netherlands) running on a HP Pavilion 9600 PC was used for image analysis. The entire image set of a single study was scaled and windowed simultaneously. The corresponding SI values of a set of IR images with varying TIs were used to determine the R1 values of the myocardial ROIs. Myocardial function was determined using data calculated from the SSFP movies. Following localization of the center point, the endo- and epicardial contours of the LV muscle in the short-axis images were detected and manually readjusted. A 0° starting point at the posteroseptal groove was set for each individual image in the set. Following these initial settings, the software divided the mass of the LV muscle into 16 segments where each individual segment was perpendicular to the centerline.

Function and ΔR1 Data Analysis

The MASS program calculated cardiac function data, such as the difference between the end-systolic and end-diastolic wall thickness (i.e., wall thickening (WT)), and the displacement of the end-systolic endocardial contour (i.e., wall motion (WM)). SI data for each ROI were also measured using MASS. WT and MRI SI data were derived from the same myocardial volume elements. Corresponding data tables of WT and SI were then generated for the entire image set and processed. An R1 value was calculated for each individual ROI to generate an R1 map. The R1 enhancement induced by CA ($\Delta R1_{ca}$) in a given pixel is proportional to the concentration of the CA in the voxel represented by that pixel, as defined by

$$\Delta R1_{ca} \propto r_1 \cdot [CA] \quad (3)$$

where r_1 is the relaxivity of the CA. This CA concentration is perfusion-dependent, and thus the ΔR1 value of a given pixel is proportional to the perfusion in its voxel. The observed relaxation rate ($R1_{obs}$) of a given pixel in the presence of the CA is the sum of the control relaxation rate $R1_0$ obtained in the absence of the CA and the relaxation rate enhancement $\Delta R1_{ca}$ induced by the CA. Therefore,

$$\Delta R1_{ca} = R1_{obs} - R1_0 \quad (4)$$

Thus, sectors with ΔR1 values larger than 0.8 sec^{-1} represented nonischemic, remote sectors ($\Delta R1_{car}$).

To eliminate differences in R1 data among the individual dogs due to potential differences in effective CA tissue uptake, all ΔR1 values were normalized to the average of the ΔR1 values observed in the remote areas ($\Delta R1_{car}$) in each individual dog:

$$\Delta R1_n = \Delta R1_{ca}/\Delta R1_r \quad (5)$$

In comparison with corresponding MP values, sectors with $\Delta R1_n \leq 80\%$ were considered to represent ischemic ROIs ($\Delta R1_{cal}$).

The calculated values were compiled as a function of anatomical position. These normalized $\Delta R1_n$ data from all ROIs in a given dog constitute the R1-enhancement map ($\Delta R1_n$), which represents the myocardial perfusion distribution.

Regional Function Analysis

A regional function map corresponding to the $\Delta R1_n$ map was generated. The myocardial function of each individual sector was also compared with the corresponding myocardial perfusion and $\Delta R1_n$ data.

Pixel-by-Pixel Image Analysis

To determine the $\Delta R1_n$ values in the myocardium with a higher spatial resolution, a series of eight superimposable 60 pixel by 60 pixel image sections containing the LV were selected from the MR images acquired with the eight different TIs. An automated algorithm was applied to determine the R1 value in each voxel associated with each pixel, using Eq. [2].

Perfusion Map

The relaxation rate, consequently the $\Delta R1_n$, of a given pixel is proportional to the concentration of the CA. This concentration is perfusion dependent, and thus the $\Delta R1_n$ value of a given pixel is proportional to the perfusion. Based on this correlation, the pixel-by-pixel $\Delta R1_n$ map can be transformed into a pixel-by-pixel perfusion map (PM).

Percent Perfusion Map (PPM)

To establish a scale to convert $\Delta R1_n$ values to perfusion values, the pixel with the maximum $\Delta R1_n$ value ($\Delta R1_{nmax}$) in that myocardium is sought. To calculate the exact percent perfusion value in each individual voxel, the following derivation applies:

$$\Delta R1_{nmax} \propto Perfusion_{max}$$

$$\Delta R1_{nmin} \propto Perfusion_{min} \quad (6)$$

$$\Delta R1_n \propto Perfusion$$

$$\Delta R1_n/\Delta R1_{nmax} - Perfusion/Perfusion_{max}$$

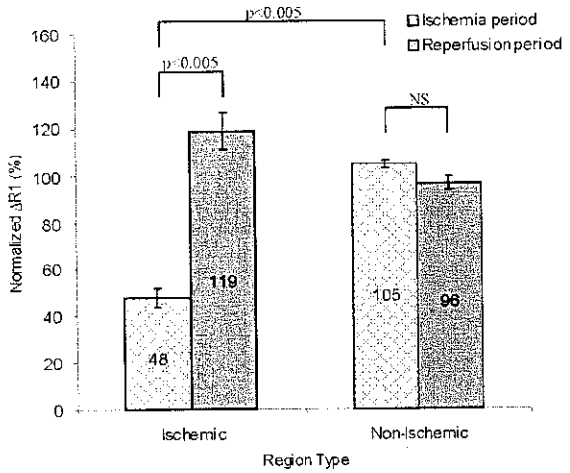

Figure 3. Average ΔR1 values of ischemic and nonischemic sectors normalized to the ΔR1 values measured during the ischemic period in the remote sectors.

$$\text{Perfusion} = (\Delta R1_n/\Delta R1_{nmax})\cdot\text{Perfusion}_{max} \quad (7)$$

Thus, to express the perfusion in any given voxel as a percent of the maximum perfusion in a particular LV, a percent perfusion (PP) parameter is calculated from Eq. [5]:

$$PP = (\Delta R1_n/\Delta R1_{nmax})\cdot 100 \quad (8)$$

The matrix containing the PP values of all voxels then yields the PPM. All pixels with negative values were rounded to zero.

Statistical Analysis

Data were analyzed using SigmaStat version 3.0 (SPSS, Inc.). Details of the statistical analysis performed for each type of results are given below.

RESULTS

Figure 3 depicts the mean ± standard error of means of $\Delta R1_n$ values calculated in ischemic (N = 47) and nonischemic (N = 94) sectors of the 11 dogs. By normalizing the ΔR1 values (see Materials and Methods section), all of the $\Delta R1_n$ values obtained in the 11 dogs were made animal-independent and thus comparable. Following CA administration, during the ischemia period a significant $\Delta R1_n$ difference was found between the ischemic and nonischemic ROIs by the Mann-Whitney rank test ($P < 0.001$). Upon reperfusion, the difference not only decreased, but due to likely hyperemia and a consequently higher CA concentration in the previously ischemic myocardium, the $\Delta R1_n$ value increased in these areas compared to the nonischemic areas. This difference, however, was not significant.

A typical image set from which $\Delta R1_n$ values were obtained is shown in Fig. 4. These images of a single LV tomographic slice were acquired with the eight different TIs. In images acquired with TIs below the contrast reversal point, reverse contrast is observed between the well perfused and ischemic regions, and the ischemic region is brighter than the nonischemic regions. The minimum contrast occurs at ~400 msec between the ischemic and nonischemic regions. At TIs above 400 msec, the contrast becomes positive, i.e. the ischemic region is darker and the well-perfused region is

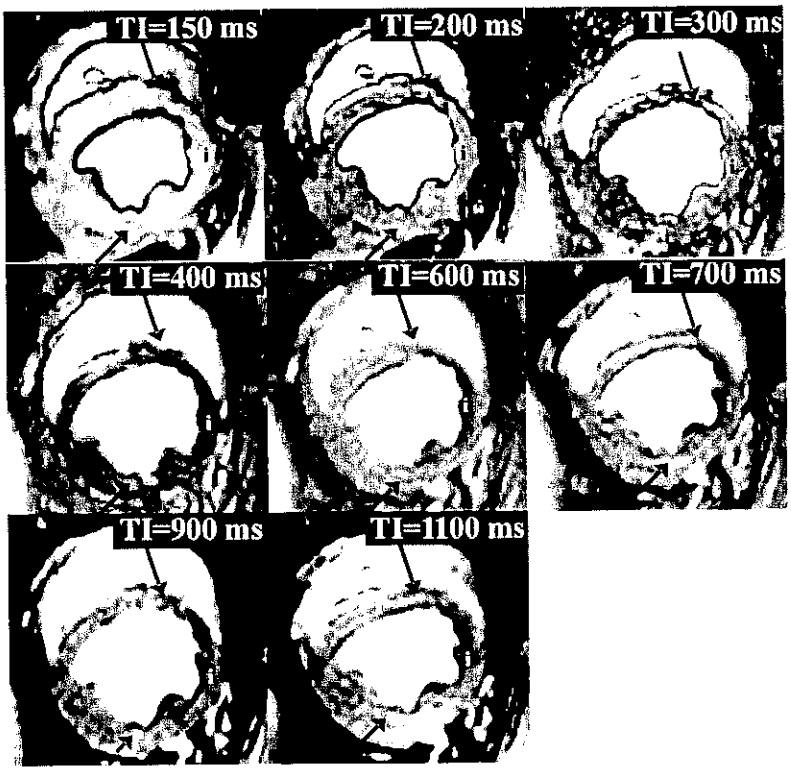

Figure 4. Representative LV images in a single slice from one dog, acquired with a series of eight TIs varying from 150 to 1100 msec. Arrows point to the edges of the ischemic region. The ischemic region is labeled with a black or white "i".

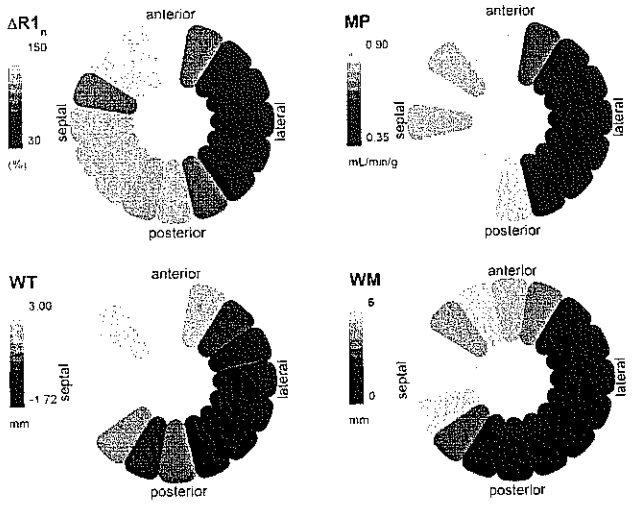

Figure 5. Each rosette illustrates one of the maps (ΔR1, MP, WT, and WM) as a function of the position of a given myocardial sector. Similar grayscales for all parameters were applied to emphasize the correspondence among the parameters.

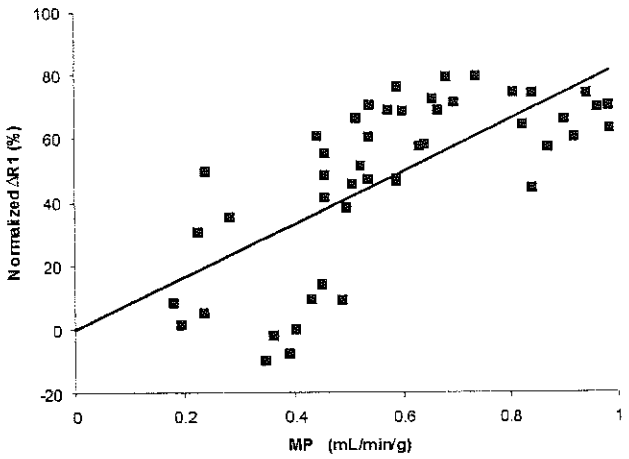

Figure 7. Normalized ΔR1 as a function of MP in all ischemic sectors evaluated in 11 dogs. The regression line was y = 82.27x + 0.04.

brighter. The maximum contrast is observable in images acquired with TIs between 600 and 900 msec.

In Fig. 5 the $\Delta R1_n$, WT, and WM maps of the same single tomographic slice from one of the dogs are shown along with the corresponding MPs. To illustrate the correspondence among the $\Delta R1_n$ map, myocardial

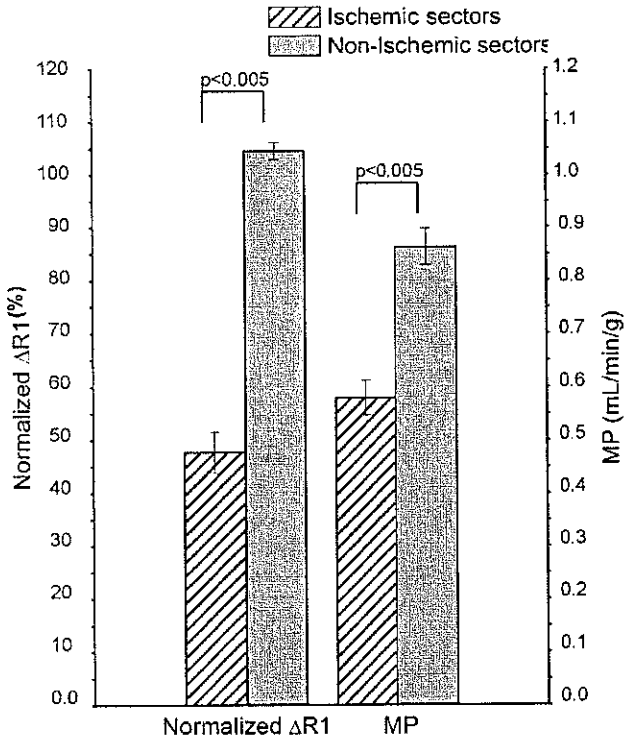

Figure 6. Mean values of MP and $\Delta R1_n$ during ischemia are shown. The error bars indicate the standard error of the mean (SEM) calculated by using the total number of ischemic and nonischemic sectors.

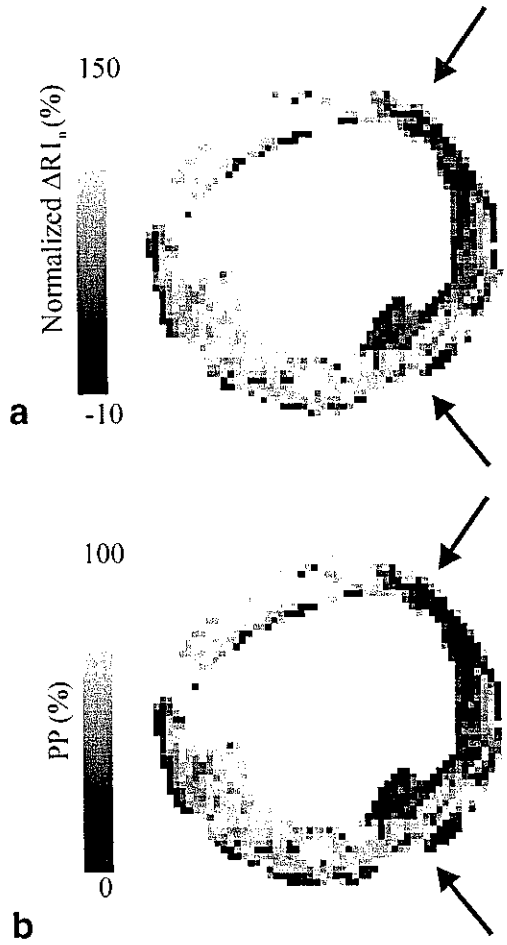

Figure 8. a: Calculated pixel-by-pixel $\Delta R1_n$ map of the LV. The arrows indicate the edges of the ischemic zone. **b:** Corresponding calculated pixel-by-pixel PPM. The arrows indicate the edges of the ischemic zone.

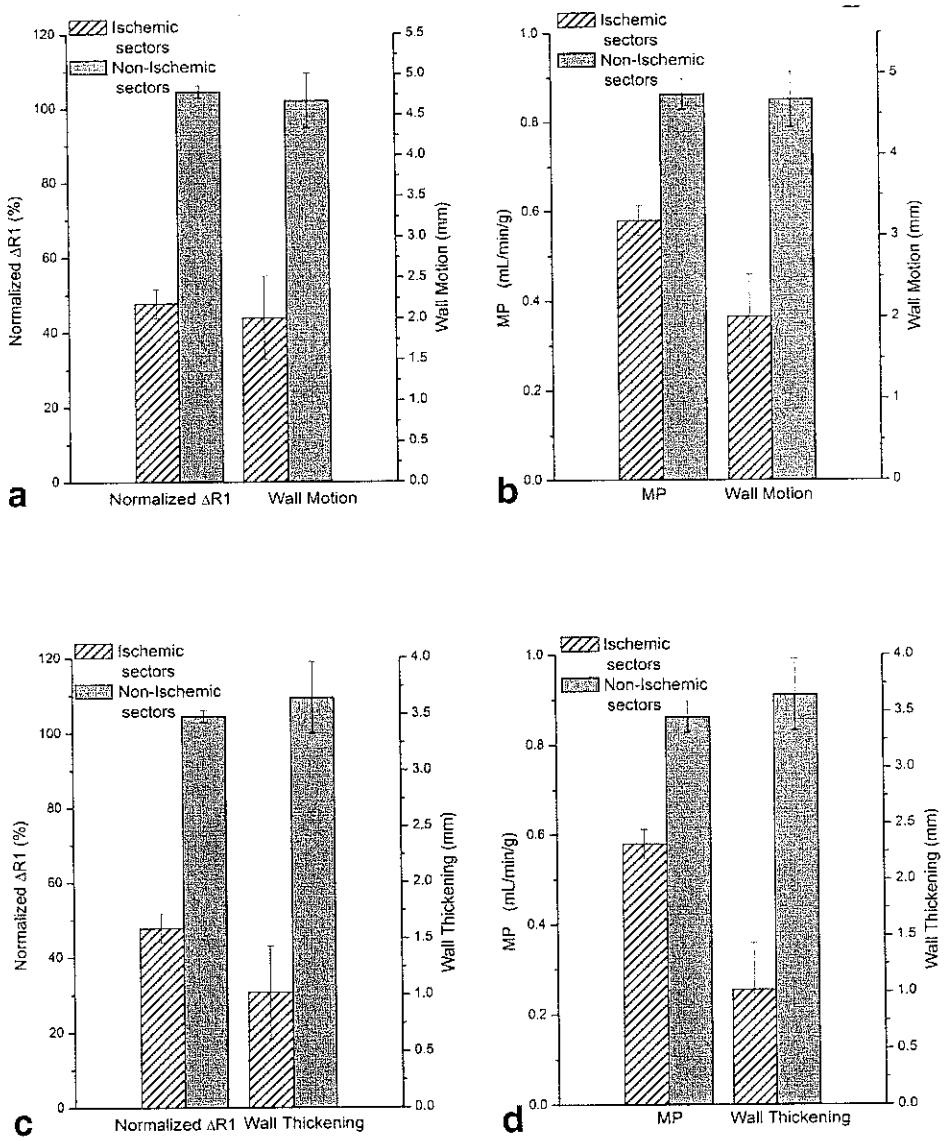

Figure 9. Mean values of $\Delta R1_n$ and WM (**a**), MP and WM (**b**), $\Delta R1_n$ and WT (**c**), and MP and WT (**d**) are shown. The error bars indicate the SEM calculated by using the total number of ischemic and nonischemic sectors from all 11 dogs. The *P* values of pairwise comparisons in ischemic sectors are shown in Table 1.

perfusion, and the two myocardial function maps, similar grayscales were used for all four parameters (Fig. 5).

In Fig. 6 bar graphs of the $\Delta R1_n$ values in ischemic and nonischemic sectors from all dogs are compared with the corresponding MP bars. A Mann-Whitney rank test was used to determine the displayed *P*-values of this comparison. In Fig. 7 the $\Delta R1_n$ data measured in the ischemic sectors of the 11 dogs are plotted as a function of the MP values in the corresponding sectors. The correlation coefficient calculated by using Pearson's product moment correlation is 0.694 ($P < 0.005$).

Based on the correlation between $\Delta R1_n$ and MP, the myocardial perfusion is calculated from the $\Delta R1_n$ values. In Fig. 8a the potential of the PPM method is demonstrated by a pixel-by-pixel resolved $\Delta R1_n$ map of a single tomographic slice. Based on validation of the correlation between $\Delta R1_n$ and MP, a pixel-by-pixel PPM was calculated in the same slice, and is shown in Fig. 8b.

The WT and WM values measured in the ischemic and nonischemic sectors are shown along with the corresponding $\Delta R1_n$ and MP values in Fig. 9.

Pairwise correlations were determined between $\Delta R1_n$ and WT, $\Delta R1_n$ and WM, and $\Delta R1_n$ and MP in all ischemic sectors evaluated in 11 dogs using Pearson's product moment correlation. The correlation coefficients and *P* values are compiled in Table 1.

Table 1
Pairwise Correlation Between $\Delta R1_n$, MP, WT, and WM Values from All Ischemic Sectors Evaluated in 11 Dogs*

Parameters	Correlation coefficient (*R*)	*P* value
$\Delta R1_n$ vs. MP	0.694	$P < 0.005$
$\Delta R1_n$ vs. WT	0.534	$P < 0.005$
$\Delta R1_n$ vs. WM	0.529	$P < 0.005$

*The statistical parameters presented here were obtained by Pearson's product moment correlation.

DISCUSSION AND CONCLUSIONS

The present study demonstrates the usefulness of normalized ΔR1 mapping using Gd(ABE-DTTA) for measuring myocardial perfusion and thus quantitatively delineating the ischemic regions in vivo. The $\Delta R1_n$ map reflects the distribution of the CA concentration in the myocardium, and thus it can not only visualize but also quantify the extent of ischemia in every ROI in the myocardium. $\Delta R1_n$ mapping visualizes R1 increases induced by a CA more effectively than the usual T1-weighted SI images. Such mapping, however, requires a CA with a myocardial lifetime that is long enough to allow the relatively long acquisitions needed for accurate determination of R1. Gd(ABE-DTTA) is a CA whose sufficiently long myocardial lifetime maintains agent concentration practically unchanged in the course of a complete set of R1 acquisitions. Therefore, with this agent it is possible to generate an accurate R1 map in a canine model of acute myocardial ischemia.

Due to the differential distribution of the CA in the ischemic vs. nonischemic myocardium, the $\Delta R1_n$ values were significantly lower in the ischemic regions than in the nonischemic regions during the ischemic period. During reperfusion, this difference vanished (Fig. 3). In the individual experiments the lower ΔR1 values showed regional correlation with the regional function parameters assessed by MRI (WT, WM), as well as with the MP values (Fig. 5). A good correspondence among the various maps is evident. The underperfused areas are clearly shown by the $\Delta R1_n$ map. Good correspondence is observed between the location of the underperfused sectors defined by the $\Delta R1_n$ map and that shown by the MP map, thus validating the former.

The difference between the mean $\Delta R1_n$ values measured in the ischemic vs. nonischemic sectors is similar to that observed between the corresponding mean MP values (Fig. 6).

In our experiments the ischemic areas became clearly delineated. In these areas a close correlation was found between the $\Delta R1_n$ and the MP values of the corresponding sectors (Fig. 7). A good correlation was observed between WT and $\Delta R1_n$ as well as the WM data vs. $\Delta R1_n$, demonstrating accurate localization of the ischemic regions by $\Delta R1_n$ mapping.

We have shown the extent to which the $\Delta R1_n$ values obtained after the injection of Gd(ABE-DTTA) reflect myocardial perfusion. Once the correlation between MP and $\Delta R1_n$ has been established, a pixel-by-pixel $\Delta R1_n$ map (Fig. 8a) can be translated into a PP map with the same resolution (Fig. 8b). It is worth mentioning that this method can provide even higher spatial resolution than the postmortem gold-standard technique, the determination of MP using colored Møs (the resolution of which is about 1 cm^3). Using the $\Delta R1_n$ map, each $\Delta R1_n$ value leading to the PP map can be obtained from a 0.014 cm^3 tomographic volume of the myocardium. Using a color scale spread between the minimum and maximum values found in the slice, the perfusion in each pixel in this calculated map can be clearly presented. The basis for these correlations is the fact that voxels with high perfusion values possess high CA concentrations, and consequently high $\Delta R1_n$ values.

By analyzing the mean values of the different parameters in Fig. 9, one can observe that both WT and WM show a roughly proportional difference between the ischemic and nonischemic sectors similar to that displayed by $\Delta R1_n$ and MP. As indicated by the *P*-values (Table 1), a significant correlation was observed between $\Delta R1_n$ and myocardial perfusion, as well as between each of the two function parameters and $\Delta R1_n$.

In clinical practice there is a growing need for an accurate and noninvasive method to determine acute myocardial perfusion defects. Based on its sufficiently long myocardial lifetime, Gd(ABE-DTTA) is suitable for use as a cardiac CA, and in conjunction with an $\Delta R1_n$ map can provide quantitative information about myocardial perfusion in ischemia.

ACKNOWLEDGMENTS

We thank Brandy Jewell from the Animal Resources Program for assistance during the surgical animal preparations. This study was supported by NIH grants to P.S. (R44 HL58285) and G.A.E. (RO1 HL63340).

REFERENCES

1. Arias E, Smith BL. Deaths: preliminary data for 2001. Natl Vital Stat Rep 2003; 51:1–44.
2. Schelbert H, Henning H, Rigo H, et al. Intravenous myocardial imaging performed serially early and late after acute myocardial infarction. Eur J Nucl Med 1977;2:75–83.
3. Basu S, Senior R, Dore C, Lahiri A. Value of thallium-201 imaging in detecting adverse cardiac events after myocardial infarction and thrombolysis: a follow up of 100 consecutive patients. BMJ 1996; 313:844–848.
4. Senior R, Glenville B, Basu S, et al. Dobutamine echocardiography and thallium-201 imaging predict functional improvement after revascularisation in severe ischaemic left ventricular dysfunction. Heart 1995;74:358–364.
5. Shiozaki H. [Diagnosis of myocardial infarction by cine MR imaging—a comparative study with thallium-201 myocardial SPECT]. Nippon Igaku Hoshasen Gakkai Zasshi 1993;53:11–22.
6. Sa Pinto P, Machado R, Pereira M, et al. [Iatrogenic vascular injuries]. Acta Med Port 2000;13:39–42.
7. Alonso M, Tascon J, Hernandez F, et al. [Complications with femoral access in cardiac catheterization. Impact of previous systematic femoral angiography and hemostasis with VasoSeal-ES collagen plug]. Rev Exp Cardiol 2003;56:569–577. [Span]
8. Wilke N, Jerosch-Herold M, Zenovich A, Stillman A. Magnetic resonance first-pass myocardial perfusion imaging: clinical validation and future applications. J Magn Reson Imaging 1999;10:676–685.
9. Kraitchman D, Chin B, Heldman A, et al. MRI detection of myocardial perfusion defects due to coronary artery stenosis with MS-325. J Magn Reson Imaging 2002;15:149–158.
10. Fieno DS, Shea SM, Li Y, et al. Myocardial perfusion imaging based on the blood oxygen level-dependent effect using T2-prepared steady-state free-precession magnetic resonance imaging. Circulation 2004;110:1284–1290.
11. Saeed M. New concepts in characterization of ischemically injured myocardium by MRI. Exp Biol Med 2001;226:367–376.
12. Al-Saadi N, Nagel E, Gross M, et al. Noninvasive detection of myocardial ischemia from perfusion reserve based on cardiovascular magnetic resonance. Circulation 2000;101:1379–1383.
13. Krombach GA, Saeed M, Higgins CB, et al. Contrast-enhanced MR delineation of stunned myocardium with administration of $MnCl_2$ in rats. Radiology 2004;230:183–190.
14. McNamara MT, Higgins CB, Ehman RL, et al. Acute myocardial ischemia: magnetic resonance contrast enhancement with gadolinium-DTPA. Radiology 1984;153:157–163.
15. Schmitt M, Horstick G, Petersen S, et al. Quantification of resting myocardial blood flow in a pig model of acute ischemia based on first-pass MRI. Magn Reson Med 2005;53:1223–1227.

16. Pomeroy O, Wendland M, Wagner S, et al. Magnetic resonance imaging of acute myocardial ischemia using a manganese chelate, Mn-DPDP. Invest Radiol 1989;24:531–536.
17. Wacker C, Wiesmann F, Bock M, et al. Determination of regional blood volume and intra-extracapillary water exchange in human myocardium using Feruglose: first clinical results in patients with coronary artery disease. Magn Reson Med 2002;47:1013–1016.
18. Canet E, Janier M, Revel D. Magnetic resonance perfusion imaging in ischemic heart disease. J Magn Reson Imaging 1999;10:423–433.
19. Johansson L, Nolan M, Taniuchi M, et al. High-resolution magnetic resonance coronary angiography of the entire heart using a new blood-pool agent, NC100150 injection: comparison with invasive x-ray angiography in pigs. J Cardiovasc Magn Reson 1999;1:139–143.
20. Amano Y, Herfkens R, Shifrin R, et al. Three-dimensional cardiac cine magnetic resonance imaging with an ultrasmall superparamagnetic iron oxide blood pool agent (NC100150). J Magn Reson Imaging 2000;11:81–86.
21. Gerber BL, Garot J, Bluemke DA, et al. Accuracy of contrast-enhanced magnetic resonance imaging in predicting improvement of regional myocardial function in patients after acute myocardial infarction. Circulation 2002;106:1083–1089.
22. Wolf G. Role of magnetic resonance contrast agents in cardiac imaging. Am J Cardiol 1990;66:59F–62F.
23. Atkinson D, Burstein D, Edelman R. First-pass cardiac perfusion: evaluation with ultrafast MR imaging. Radiology 1990;174:757–762.
24. Manning W, Atkinson D, Grossman W, et al. First-pass nuclear magnetic resonance imaging studies using gadolinium-DTPA in patients with coronary artery disease. J Am Coll Cardiol 1991;18:959–965.
25. Boudraa A, Behloul F, Janier M, et al. Temporal covariance analysis of first-pass contrast-enhanced myocardial magnetic resonance images. Comput Biol Med 2001;31:133–142.
26. Covarrubias DJ, Rosen BR, Lev MH. Dynamic magnetic resonance perfusion imaging of brain tumors. Oncologist 2004;9:528–537.
27. Simor T, Chu W-J, Johnson L, et al. In vivo MRI visualization of acute myocardial ischemia and reperfusion in ferrets by the persistent action of the contrast agent Gd(BME-DTTA). Circulation 1995;92:3549–3559.
28. Saab-Ismail N, Simor T, Gaszner B, et al. Synthesis and in vivo evaluation of new contrast agents for cardiac MRI. J Med Chem 1999;42:2852–2861.
29. Simor T, Gaszner B, Saab N, et al. Gd(ABE-DTTA)-enhanced high resolution cardiac MRI for the diagnosis of acute myocardial ischemia. In: Proceedings of the 13th World Congress of Cardiology. Rio de Janeiro, Brazil, 1998. p 865–869.
30. Simor T, Gaszner B, Oshinski J, et al. Gd(ABE-DTTA)-enhanced cardiac MRI for the diagnosis of ischemic events in the heart. J Magn Reson Imaging 2005;21:536–545.
31. Kaldoudi E, Williams SCR. Relaxation time measurements in NMR imaging. Part I: Longitudinal relaxation time. Concepts Magn Reson 1993;5:217–242.